Proceedings of IMECE2002
ASME International Mechanical Engineering Congress & Exposition
November 17-22, 2002, New Orleans, Louisiana

IMECE2002-33779

MASS FLOW MEASUREMENTS OF GASES IN DEEP-RIE MICROCHANNELS

Jaesung Jang, Yabin Zhao, Steven T. Wereley, and Lichuan Gui
Mechanical Engineering, Purdue University
West Lafayette, IN 47907-1288
Tel: 1-765-494-5624, Fax: 1-765-494-0539, E-mail: wereley@purdue.edu

ABSTRACT

We present mass flow measurements and pressure distributions in near unity aspect ratio microchannels using Deep Reactive Ion Etching (RIE). Almost all of the previous papers have dealt with only wide channels for gas flow measurements. We also adopt Spin-On-Glass (SOG) to bond Pyrex glass to silicon. Using the first order slip flow formula and experimental data, we extracted the tangential momentum accommodation coefficient (TMAC) of 0.425 for the case of SOG and Si microchannels and air, and the effective diameter of 57.67µm. Increased mass flow from the incompressible flow case is mostly due to compressibility rather than rarefaction, which is expected from the fact that the Knudsen number is 0.00115, the borderline of slip flows. The deviations from the linear incompressible pressure distributions get larger with increasing inlet pressures, and the dimensionless streamwise locations of maximum deviations are between 0.5 and 0.6, which is slightly downstream from the middle of the channels. It is notable that these experimental data are much closer to simulation results than the previous experiments in microchannels. The inlet pressure drops are almost linear with respect to pressure ratio of inlet to outlet. This type of near unity aspect ratio microchannel is more effective for heat exchangers than previous thin, wide channels.

KEYWORDS: pressure distributions, near unity aspect ratio, Deep-RIE microchannel, mass flow measurements.

INTRODUCTION

During the last few decades, rapid progress in micromachining technology has made it possible to fabricate micron-sized mechanical systems such as microchannels for industrial applications and scientific research. The microchannel is one of the simplest and most common components in microfluidic and micro heat transfer systems. To date, several experiments and numerical simulations in microchannels and microducts have been published. These are summarized in [1-2].

Pfahler et al. [3] and Harley et al. [4] presented some of the first analytic and experimental work on rarefied microchannel flows [5] and demonstrated that slip flow exists in micromachined channels via the differences of Poiseuille numbers in no-slip flow and slip flow. They fabricated shallow channels by RIE and deeper microchannels using wet etching. Wet chemical etching is considered to be less precise than dry etching with respect to minute dimensional control [6].

Pong et al. [7] and Liu et al. [8] presented the first experimental data on the pressure distribution along microchannels using an array of surface micromachined pressure sensors. In their experiments they showed that nonlinear pressure distributions exist in the microchannels due to compressibility effects. Subsequent experiments by Shih et al. [9] presented mass flow measurements and pressure distributions. Those data were not in agreement with any theory [5, 10].

Arkilic et al. [11] presented a two-dimensional analysis of the Navier-Stokes equations with the first order slip-velocity boundary condition in high aspect ratio microchannels, which were fabricated with selective oxidation and silicon direct bonding to make the same surface along the channel. They also presented an accurate way of measuring mass flow rates as small as the order of sub-nanomol per second [12]. Other papers of theirs [5, 13] empirically measured effective diameters and TMACs of some gases in the microchannels at the more standard conditions using the first order slip flow solution. However, their measurements were restricted to flow rates and pressure drops at the inlet and outlet, although pressure distribution in microchannels is one of the most important parameters for understanding the microflow.

Practically speaking, near unity aspect ratio microchannels are more effective in Very Large Scale Integrated (VLSI) circuit cooling, one of the most popular microchannel applications [14-15]. But, the aforementioned papers all have dealt with only wide channels, or high aspect ratio channels for gas flow measurements. To date, there has not been a paper dealing with near unity aspect ratio microchannels using Deep RIE for gas flow measurements; The Deep RIE process has

 Copyright © 2002 by ASME

become more popular in recent years. Therefore, we will present mass flow rates as well as pressure distributions in the microchannels. Further, we adopt SOG to bond Pyrex glass to silicon in the microchannels. The bonding has several benefits over anodic bonding such as lower bonding temperature, no applied voltage, and less sensitivity to surface roughness. In addition, the transparency of the SOG film makes possible flow visualization like micro-PIV [16].

ANALYSIS OF EXPERIMENTAL DATA

To model the flow, it is assumed that the flow in the rectangular microchannel is one-dimensional isothermal flow at steady state and can be approximated as a circular duct with an appropriate hydraulic diameter. For relatively low Reynolds (*Re)* flow in the microchannel with large ratio of channel length to diameter, the inertia effects in the momentum equations can be neglected [10]. In addition, we cannot assume the flow is incompressible because large-pressure drops can be produced by viscous dissipation in the microchannel even at Mach (*Ma*) numbers much less than 0.3 [1, 10].

An appropriate set of governing equations is simplified as

$$\frac{\partial p}{\partial x}=\frac{\mu}{r}\frac{\partial}{\partial r}\left(r\frac{\partial u}{\partial r}\right) \qquad (1)$$

$$\nabla\cdot(\rho u)=0 \qquad (2)$$

$$p=\rho R_s T \qquad (3)$$

where p is pressure, x is the streamwise distance from the inlet, μ is dynamic viscosity, u is the streamwise velocity component, ρ is density of air, R_s is specific gas constant for air, and T is temperature of the channel and air. The slip boundary condition and symmetry condition can be written as

$$u\Big|_{r=r_o}=-\frac{2-f}{f}\lambda\left(\frac{\partial u}{\partial r}\right)\Big|_{r=r_o} \qquad (4)$$

$$\frac{\partial u}{\partial r}\Big|_{r=0}=0 \qquad (5)$$

where r_o is half of the hydraulic diameter (D_h), λ is the mean free path of air and f is TMAC. Thermal creep effect is not included in the slip boundary condition because we assume constant temperature along the microchannel. The streamwise velocity component is then derived from Eq. (1) with those boundary conditions applied as

$$u(r)=\frac{1}{4\mu}\frac{dp}{dx}\left(r^2-r_o^2-4r_o^2\,Kn(x)\frac{2-f}{f}\right) \qquad (6)$$

where $Kn(x)$ is local Knudsen number ($=\lambda(x)/D_h$).

We now can the get mass flow rate and pressure distribution by applying the ideal gas law and the relationship between pressure and local Knudsen number at constant temperature, $Kn(x)p(x) = Kn_o p_o$.

$$\dot{m}=\int_0^{r_o}\rho\,2\pi r\,u\,dr =\frac{p(x)}{R_sT}\frac{\pi}{\mu}\frac{dp}{dx}\frac{(-r_o^4)}{8}\left(1+8\frac{2-f}{f}\frac{Kn_o p_o}{p(x)}\right) \qquad (7)$$

For constant mass flow, we integrate Eq. (7), which is a separable equation, on both sides with respect to differential pressure and streamwise variable. We get pressure distribution, Eq. (8), along the microchannel by finding roots for the second order polynomial equation obtained from the integration above. Then we choose one of the two roots, because the other does not have any physical meaning.

$$p^*(\xi)=-8\frac{2-f}{f}Kn_o+\left[\left(8\frac{2-f}{f}Kn_o\right)^2+1+16\frac{2-f}{f}Kn_o+\frac{16\dot{m}\mu R_sLT}{\pi r_o^4 p_o^2}(1-\xi)\right]^{1/2} \qquad (8)$$

where ξ *(=x/L)* is dimensionless distance from the inlet, L is the channel length, and $p^*(\xi)(=p(\xi)/p_o)$ is dimensionless pressure at ξ.

If we substitute 0 for ξ in Eq. (8), mass flow rate can be derived as

$$\dot{m}=\frac{\pi r_o^4 p_o^2}{16\mu R_sLT}\left[\Pi^2-1+16\frac{2-f}{f}Kn_o(\Pi-1)\right] \qquad (9)$$

where p_o is outlet pressure, Kn_o is outlet Knudsen number, and Π is pressure ratio of inlet to outlet ($\Pi = p_i/p_o$).

The power of four in the radius of the mass flow rate and the pressure distribution means that they are very sensitive to channel size measurements. We derive the formulas for empirically extracting effective diameters and TMACs via the same procedure as Arkilic et al. [13]. Given the slope of flow conductance on the left term of the Eq. (10) with respect to the average of the inlet and outlet pressures, we can find two times r_o, or effective diameter (D_e).

$$\frac{\dot{m}}{p_i-p_o}=\frac{\pi r_o^4}{8\mu R_sLT}\frac{p_i+p_o}{2}+\frac{\pi r_o^4}{\mu R_sLT}\frac{2-f}{f}Kn_o p_o \qquad (10)$$

where p_i is inlet pressure. We also can get the TMAC, f from the slope of normalized flow rate on the left of Eq. (11) with respect to the reciprocal of the average pressure and half of the effective diameter above.

$$\frac{\dot{m}}{p_i^2-p_o^2}=\frac{\pi r_o^4}{2\mu R_sLT}\frac{2-f}{f}Kn_o p_o\frac{2}{p_i+p_o}+\frac{\pi r_o^4}{16\mu R_sLT} \qquad (11)$$

CHANNEL FABRICATION AND EXPERIMENTAL SETUP

The microchannel chip (8 x 8 mm^2) consists of the main microchannel, inlet and outlet anisotropically etched with Tetra-Methyl-Ammonium Hydroxide (TMAH), five reservoirs for measuring the pressure along the main microchannel, and short, narrow channels connecting the main microchannel with the reservoirs (Fig.1). The main microchannel is 100.5μm wide, 40.53μm deep, and 5020μm long.

The fabrication procedure is straightforward as shown in Fig. 2. We begin with 525-μm-thick P type (100) 4-in. silicon wafers. Initial 6000Å thick thermal oxide is grown on both sides. The microchannels and pressure measurement reservoirs on the frontside are defined by photolithography followed by the oxide removal. Then Deep RIE (Bosch Process) is applied to form the microchannels and pressure measurement reservoirs. The wafers are oxidized again for the barrier of next wet etching of TMAH. The oxide for input and output holes is then etched on the backside keeping the frontside oxide safe. We use photoresist bonding [17] for protecting the frontside

Copyright © 2002 by ASME

oxide during the backside patterning because normal spin coating on the frontside is not possible due to large depth of the microchannel. We etch Si on the backside with 20 wt. % TMAH at 90 °C for 10.5 hours to the bottom surface of the reservoirs. The remaining oxide is then removed and the wafers are diced.

Finally we use low melting temperature SOG (Methyl-silsesquioxane 400F from Filmtronics Inc., Pennsylvania, USA) as an adhesive of Pyrex 7740 glasses with the diced microchannel chips. The SOG is flowable at 150 °C-210 °C and is applicable to microfluidic chips with rough surfaces. After cleaning glass chips, SOG film is coated on them at 5000 rpm for 40 seconds and dried in a convection oven at 90 °C for 2 min. Then the glass chips are manually clamped with the microchannel chips and the assembly is kept at 200 °C for 2 hours on a hotplate [16].

The bonded chips are optically inspected to determine if the SOG film completely seals the microchannel. The film

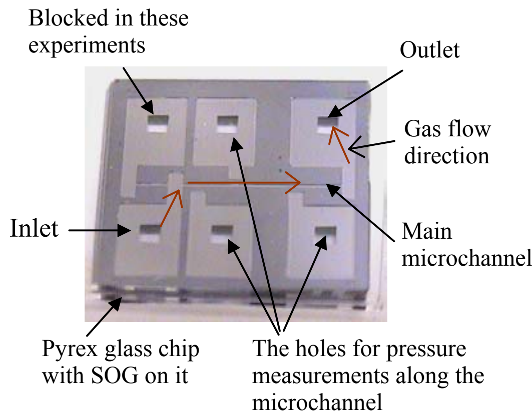

Figure 1. Schematic of the microchannel chip

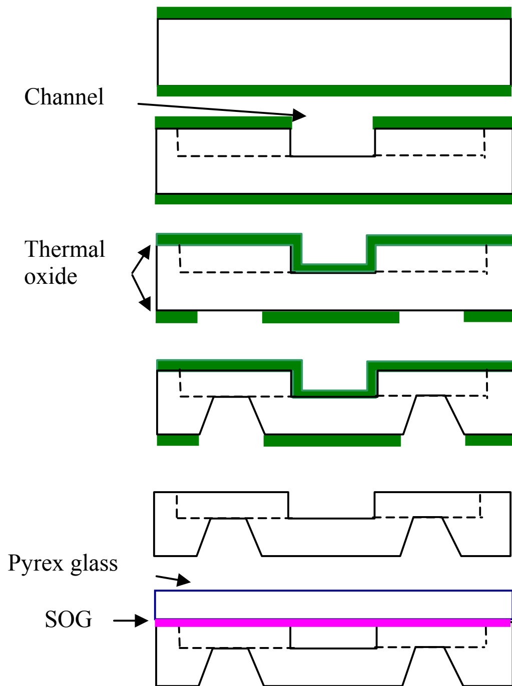

Figure 2. Fabrication procedure

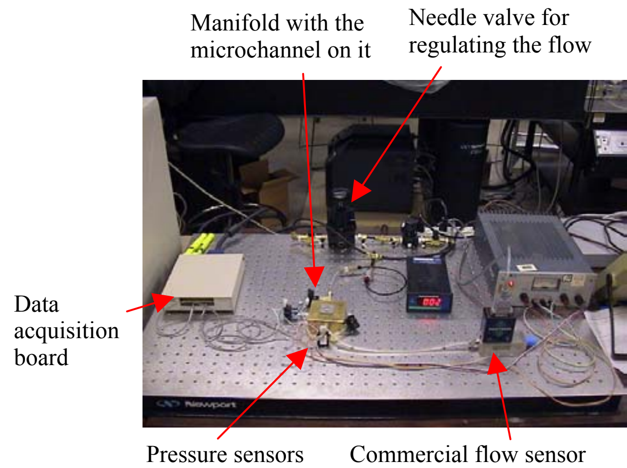

Figure 3 Experimental set up

thickness is 3000Å according to the datasheet from Filmtronics Inc.. We measure the roughness of the cured film with a profilometer (Alpha-step 200) and it has an average surface roughness (RA) of 72.7Å. The bottom surface due to the Deep RIE in the microchannel has average roughness of 97.1Å and relative roughness with respect to hydraulic diameter (= RA/D_h) of 1.68 x 10^{-4}. Additionally the root mean square roughness of the sidewall is reported to be less than 350Å due to the Deep RIE [18].

Figure 3 shows experimental set up. When beginning experiments, we verify that there are no leaks by putting all the joints into a water vessel, pressurizing them, and observing whether or not bubbles come out. Next we apply compressed air to the inlet of the microchannels keeping the outlet at one atmosphere. At steady state we record pressures at five different points along the microchannels and mass flow rates through them via a data acquisition board (NI PCI-MIO-16E-4). Pressures and mass flow rates are measured by pressure sensors (Omega PX138) and a high precision mass flow sensor (Hastings HFM300) respectively. The pressure sensors have accuracy of maximum +/- 0.5% FS, where the FS is 5 psig and the flow sensor has +/- 0.75% FS, where the FS is 5 sccm. We also test the pressure drop in the passage of the manifold by connecting it with a microchannel with very small flow resistance, and it is found to be negligibly small.

Table 1. Experimental conditions and physical properties of air

Parameter	Range or Mean values
Outlet pressure (p_o)	101.318 kPa
Pressure ratio (Π)	1.01 - 1.21
Mean free path (λ)	66.3 nm
Outlet Knudsen number (Kn_o)	1.15 x 10^{-3}
Temperature (T)	298 K
Molecular mass	28.96
Outlet Mach number (Ma_o)	0.0013 - 0.0527
Reynolds number (Re)	1.8 - 69.4
Specific gas constant (R_s)	287 J/kg K
Ratio of specific heats (γ)	1.4
Molecular diameter	3.712 Å
Dynamic viscosity (μ)	180.0 x 10^{-3}Ns/m^2

Copyright © 2002 by ASME

RESULTS AND DISCUSSION

Table 1 summarizes the experimental conditions and physical parameters for air. A hard sphere model is used to calculate the effective molecular diameter. This procedure is commonly used despite fact that it is reported to be slightly different from real gases [19].

Figures 4 and 5 indicate the flow conductance as a function of the average pressure to extract the effective diameter using the Eq. (10) and normalized flow rates with reciprocal of average pressure to get TMACs with Eq. (11) respectively. Generally the TMAC depends on both surface conditions and gas type, and most of the previously measured TMACs were obtained under very special conditions, such as vacuum facilities [5]. For that reason, TMAC for the case of air, and SOG and silicon surfaces at atmospheric conditions are not available. Figure 4 uses the highest twelve pressure points for a more reliable calculation, where R^2 is 99.4%, because of the large scatter in the lower pressure range as shown in the Fig. 5. The error bars indicate 95% confidence intervals. We find an effective diameter of 57.67μm while the geometrically determined hydraulic diameter is 57.76μm. The extracted TMAC is 0.425 for this case.

Figure 6 shows the measured mass flow rates as a function of the pressure ratio of inlet to outlet. The square symbols represent the readings from the mass flow sensor, while the solid line is calculated from the Eq. (9) using the effective diameter and the extracted TMAC. This is very close agreement between the measurements and prediction by the slip flow formula. The short dashed line and the long dashed line indicate Eq. (9) with the outlet Knudsen number of zero and Hagen-Poiseuille flow respectively. Increased mass flow from the incompressible flow case is mostly due to compressibility rather than rarefaction, which is expected from the fact that the Knudsen number of 0.00115 is near the borderline of slip flows [1].

Figure 7 indicates the pressure distributions along the microchannel for a series of mass flow rates. We observe their nonlinearity and small pressure drops at the inlet. To make this nonlinearity more apparent, deviations from the linear incompressible pressure distribution between the second and the fifth point from the inlet of Fig. 7 are shown in Fig. 8 with curves fitted with the spline function at Excel. From this graph it is apparent that the deviations increase with increasing inlet pressures, which means compressibility effects become more

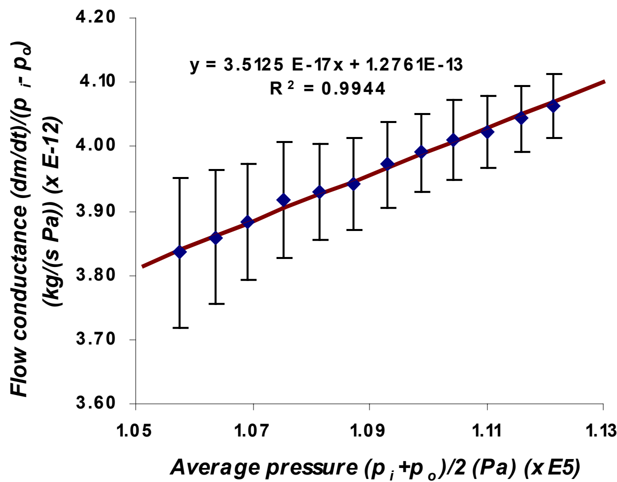

Figure 4. Flow conductance with average pressure

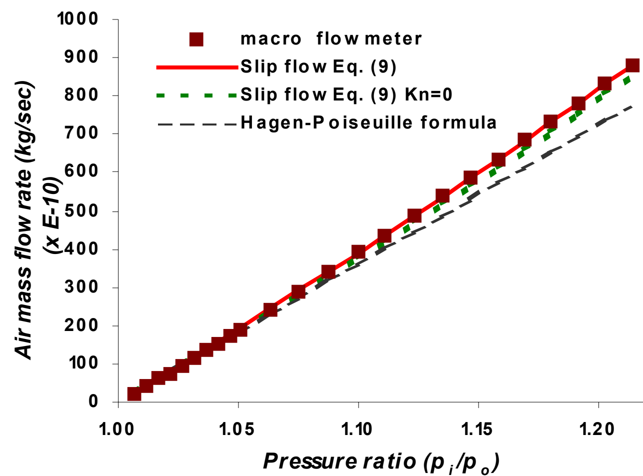

Figure 6. Measured mass flow rate with inlet pressure ratio

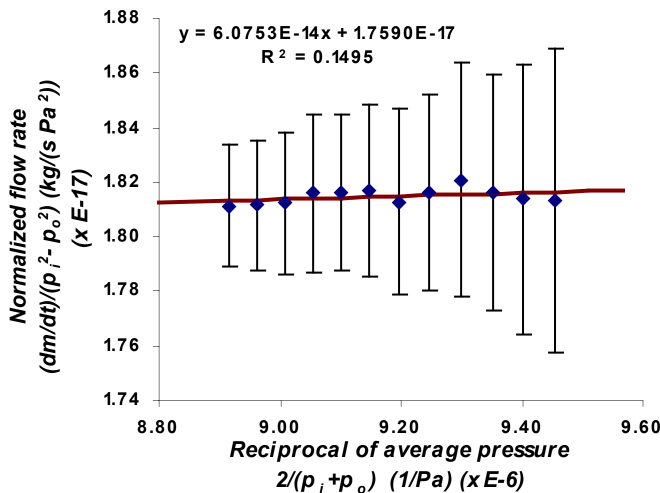

Figure 5. Normalized flow rate with the reciprocal of average pressure

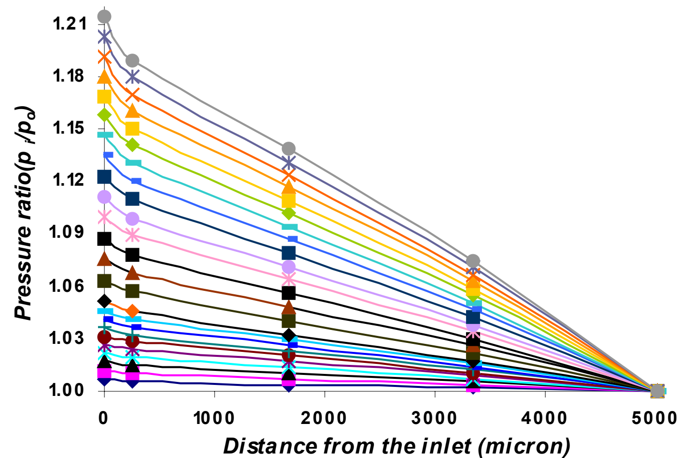

Figure 7. Pressure distribution along the microchannel

Copyright © 2002 by ASME

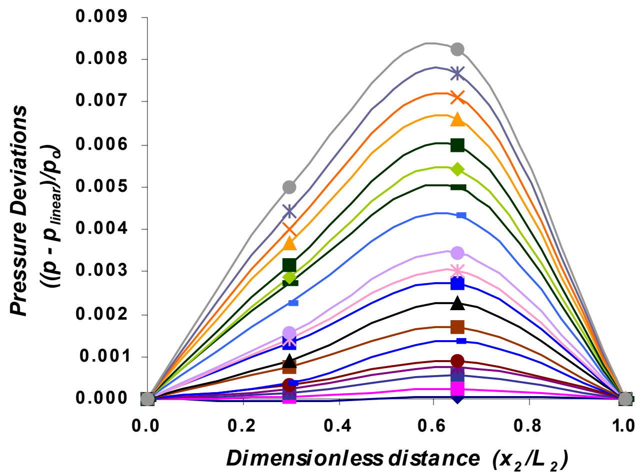

Figure 8. Pressure deviations from the linear pressure distribution between the second from the inlet of Fig. 7 and the outlet, where L_2 is the distance from the second to the outlet and x_2 is the streamwise distance from the second.

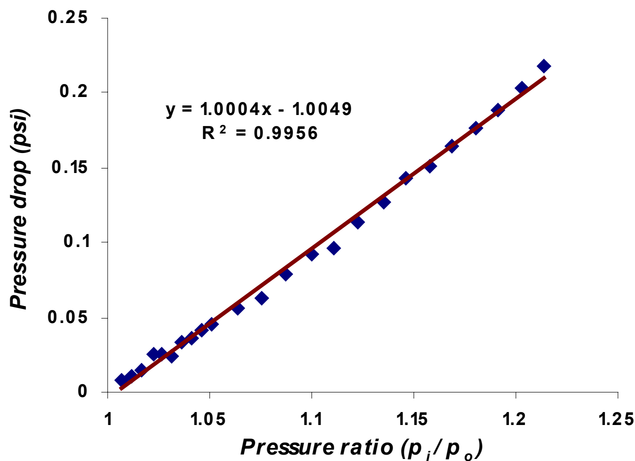

Figure 9. Inlet pressure drop at the inlet as a function of inlet pressure ratio

pronounced as the inlet pressure ratio increases. The dimensionless locations for the maximum deviations are between 0.5 and 0.6, which is a bit skewed downstream from the middle. It is notable that the locations of the maximum in these experimental data are much closer to those of the simulation results, 0.55 [10]. The experiments of Pong et al. have a maximum at 0.4 [10] and have been the most frequently cited experimental data for the pressure distribution in uniform and straight microchannels.

Figure 9 shows inlet pressure drops as a function of the pressure ratio of inlet to outlet. The pressure drops are obtained by subtracting the extrapolated values at the inlet assuming there are no entrance effects from the real inlet pressures. The pressure drops can be considered to be linear, which is easier to calibrate in flow sensor applications.

CONCLUSIONS

We present mass flow measurements as well as pressure distributions in near unity aspect ratio microchannels using Deep RIE. We adopt SOG to bond Pyrex glass to silicon chips, which has some benefits over anodic bonding such as lower bonding temperature, no applied voltage, and less sensitivity to surface roughness. In addition, the transparency of the SOG film makes possible flow visualization like micro-PIV. Using the first order slip formula and experimental data, we extracted the TMAC of 0.425 for the case of air, and SOG and silicon surfaces at atmospheric conditions and the effective diameter of 57.67μm despite significant scatter at the low pressure range. Increased mass flow from the incompressible flow case is mostly due to compressibility rather than rarefaction, which is expected from the fact that the Knudsen number of 0.00115 is near the borderline of slip flows [1]. Deviations from the linear incompressible distributions get larger with inlet pressure ratio, and the dimensionless axial locations of maximum deviations are in between 0.5 and 0.6, which are skewed slightly downstream of the middle of the channel. It is notable that these experimental data are much closer to the simulation results of 0.55 than those of Pong et al., 0.4 [10]. The inlet pressure drops are negligible, which makes these channels easy to calibrate for possible flow sensor applications.

ACKNOWLEDGMENTS

We authors thank to the microfabrication laboratory at Purdue University, West Lafayette. We also wish to acknowledge the financial support of the Indiana 21st Century Research and Technology Fund.

REFERENCES

[1] Gad-el-Hak, M., 1999, "The Fluid Mechanics of Microdevices—The Freemann Scholar Lecture," J. Fluids Engineering, **121**, pp. 5-33.

[2] Ho, C. -M., and Tai, Y. -C., 1998, "Micro-electro-mechanical-Systems (MEMS) and Fluid Flows," Annual Review of Fluid Mechanics, **30**, pp. 579-612.

[3] Pfahler, J., Harley, J., Bau, H., and Zemel, J. N., 1991, "Gas and Liquid Flow in Small Channels," ASME '91, DSC-**32**, pp. 49-60.

[4] Harley, J. C., Huang, Y., Bau, H. H., and Zemel, J. N., 1995, "Gas Flow in Micro-channels," J. Fluid Mechanics, **284**, pp. 257-274.

[5] Arkilic, E. B., Breuer, K. S., and Schmidt, M. A., 2001, "Mass Flow and Tangential Momentum Accommodation in Silicon Micromachined Channels," J. Fluid Mechanics, **437**, pp. 29-43.

[6] Madou, M., 1997, *Fundamentals of Microfabrication*, CRC Press.

[7] Pong, K. -C., Ho, C. -M., Liu, J., and Tai, Y. -C., 1994, " Non-linear Pressure Distribution in Uniform Microchannels," ASME '94, FED-**197**, pp. 51-56.

[8] Liu, J., Tai, Y. -C., and Ho, C. -M., 1995, "MEMS for Pressure Distribution Studies of Gases Flows in Microchannels," MEMS '95, pp. 209-215.

[9] Shih, J. C., Ho, C. -M., Liu, J., and Tai, Y. -C., 1996, "Monatomic and Polyatomic Gas Flow through Uniform Microchannels," ASME '96, DSC- **59**, pp. 197-203.

[10] Karniadakis, G. E., and Beskok, A., 2002, *Micro flows: Fundamentals and Simulation*, Springer-Verlag.

[11] Arkilic, E. B., Schmidt, M. A., and Breuer, K. S., 1997, "Gases Slip Flow in Long Microchannels," J. Microelectromechanical Systems, **6**, pp. 167-178.

Copyright © 2002 by ASME

[12] Arkilic, E. B., Schmidt, M. A., and Breuer, K. S., 1998, “Sub-nanomol per second Flow Measurement near Atmospheric Pressure,” Experiments in Fluids, **25**, pp. 37-41

[13] Arkilic, E. B., Schmidt, M. A., and Breuer, K. S., 1996, “TMAC Measurement in Silicon Micromachined Channels,” Proceedings of the Symposium on Rarefied Gas Dynamics, Beijing China.

[14] Tuckerman, D. B., and Pease, R. F. W., 1981, “High-Performance Heat Sinking for VLSI,” IEEE Electron Device Letters, EDL-**2**, pp. 126-129.

[15] Kim, M. S., Araki, T., Inaoka, K., and Suzuki, K., 2000, “Gas Flow Characteristics in Microtubes,” JSME International Journal, Series B, **43**, pp. 634-639.

[16] Gomez, R., Bashir, R., Sarakaya, A., Ladisch, M. R., Sturgis, J., Robinson, J. P., Geng, T., Bhunia, A. K., Apple, H. L., and Wereley, S. T., 2001, “Microfluidic Biochip for Impedance Spectroscopy of Biological Species,” Biomedical Microdevices, **3**, pp. 201-209.

[17] Wright, J. A., Tatic-Lucic, S., Tai, Y. –C., MaGrath, W. R., Bumble, B., and LeDuc, H., 1995, “ Integrated Silicon Micromachined Waveguide Circuits for Submillimeter Wave Applications,” Six International Symposium on Space Terahertz Technology, pp. 387-396.

[18] Chabloz, M., Sasaki, Y., Matsuura, T., and Tsutsumi, K., 2000, “Improvement of Sidewall Roughness in Deep Silicon Etching,” Microsystem Technologies, **6**, pp. 86-89.

[19] Bird, G. A., 1983, “Definition of Mean Free Path for Real Gases,” Physics of Fluids, **26**, pp. 3222-3223.

 Copyright © 2002 by ASME